Precipitation evolution in Al–Zr and Al–Zr–Ti alloys during aging at 450–600 °C

Keith E. Knipling [a,b,*], David C. Dunand [b], David N. Seidman [b,c]

[a] *Naval Research Laboratory, Code 6356, 4555 Overlook Avenue, SW, Washington, DC 20375-5320, USA*
[b] *Department of Materials Science and Engineering, Northwestern University, 2220 Campus Dr., Evanston, IL 60208-3108, USA*
[c] *Northwestern University Center for Atom-Probe, Tomography (NUCAPT), Northwestern University, 2220 Campus Dr., Evanston, IL 60208-3108, USA*

Abstract

The transformation of Al_3Zr ($L1_2$) and $Al_3(Zr_{1-x}Ti_x)$ ($L1_2$) precipitates to their respective equilibrium $D0_{23}$ structures is investigated in conventionally solidified Al–0.1Zr and Al–0.1Zr–0.1Ti (at.%) alloys aged isothermally at 500 °C or aged isochronally in the range 300–600 °C. Titanium additions delay neither coarsening of the metastable $L1_2$ precipitates nor their transformation to the $D0_{23}$ structure. Both alloys overage at the same rate at or above 500 °C, during which spheroidal $L1_2$ precipitates transform to disk-shaped $D0_{23}$ precipitates at ca. 200 nm in diameter and 50 nm in thickness, exhibiting a cube-on-cube orientation relationship with the α-Al matrix. The transformation occurs heterogeneously on dislocations because of a large lattice parameter mismatch of the $D0_{23}$ phase with α-Al. The transformation is very sluggish and even at 575 °C coherent $L1_2$ precipitates can remain untransformed. Mechanisms of microstructural coarsening and strengthening are discussed with respect to the micrometer-scale dendritic distribution of precipitates.
© 2007 Acta Materialia Inc. Published by Elsevier Ltd. All rights reserved.

Keywords: Aluminum alloys; Zirconium; Titanium; Precipitation strengthening; Coarsening

1. Introduction

The Al–Zr system exhibits particular promise for developing thermally-stable precipitation-strengthened Al alloys [1,2]. Upon aging, decomposition of supersaturated Al–Zr solid solutions occurs by the nucleation of Al_3Zr precipitates with a metastable cubic $L1_2$ structure (structurally and chemically analogous to the Ni_3Al (γ') phase in Ni-based superalloys [3,4]), which are thermally stable at high homologous temperatures. Fine and coworkers [5–9] have suggested that even greater stability can be achieved by decreasing the lattice parameter mismatch between Al_3Zr and the α-Al solid solution. Through ternary additions of transition metals (TM) such as Ti, V, or Hf, $Al_3(Zr_{1-x}TM_x)$

($L1_2$) precipitates are formed that are shown to exhibit reduced coarsening rates compared with that of binary Al_3Zr ($L1_2$) precipitates, which was attributed to a reduced matrix/precipitate lattice parameter mismatch [7,9–12].

In a prior study by the authors [13], the microstructures and ambient-temperature mechanical properties of conventionally solidified Al–Zr and Al–Zr–Ti alloys were studied during isothermal aging at 375, 400, or 425 °C. Pronounced hardening results from precipitation of nanometer-scale, spheroidal Al_3Zr ($L1_2$) or $Al_3(Zr_{1-x}Ti_x)$ ($L1_2$) precipitates within solute-enriched dendrites, reflecting the microsegregation of Zr and Ti solute atoms during solidification. The initial inhomogeneous supersaturation of solute atoms after solidification influences not only the spatial distribution of precipitates, but also the precipitate size and morphology, as well as the nucleation mechanism. Within the center of the dendrites, where the solute supersaturations are greatest, the intradendritic $L1_2$ precipitates are small (<10 nm radius), coherent, and homogeneously distributed

---

* Corresponding author. Address: Naval Research Laboratory, Code 6356, 4555 Overlook Avenue, SW, Washington, DC 20375-5320, USA. Tel.: +1 202 767 2947.
E-mail address: knipling@anvil.nrl.navy.mil (K.E. Knipling).

at high number densities. Interdendritic $L1_2$ precipitates between the dendrites are larger (ca. 25 nm radius) and are heterogeneously nucleated at lower number densities. Despite extended aging times (3200 h) at 425 °C ($0.75T_m$ of Al), the alloys do not overage appreciably and the metastable $L1_2$ Al_3Zr or $Al_3(Zr_{1-x},Ti_x)$ precipitates do not transform to the equilibrium $D0_{23}$ structure. The addition of Ti was shown to have no effect on the coarsening of Al_3Zr ($L1_2$) precipitates or the onset of overaging.

This article investigates similar alloys during aging at higher temperatures: (i) isothermal aging at 500 °C ($0.83T_m$); and (ii) isochronal aging from 300 to 600 °C (0.61–$0.94T_m$). Microstructural coarsening and strengthening mechanisms, with respect to the micrometer-scale dendritic distribution of precipitates, are studied, and the $L1_2 \rightarrow D0_{23}$ transformation of the Al_3Zr or $Al_3(Zr_{1-x},Ti_x)$ precipitates is discussed in detail.

2. Experimental procedures

A series of binary Al–0.1Zr and ternary Al–0.1Zr–0.1Ti (at.%) alloys were investigated; alloy designations, compositions, and aging conditions are summarized in Table 1. Small (ca. 7 g) buttons were prepared by non-consumable electrode arc melting as described previously [13]. As-cast samples were aged directly, with no prior homogenization treatment. The verified compositions in Table 1 were obtained by bulk chemical analysis performed by direct current plasma emission spectroscopy (ATI Wah Chang, Albany, OR).

To investigate the overaging behavior isothermally, peak-aged specimens of Al–0.1Zr(b) and Al–0.1Zr–0.1ZTi(b) (aged isothermally at 375 °C for 100 h to ca. 450 MPa hardness [13]) were exposed at 500 °C; overaging was monitored by Vickers microhardness measurements. The microstructures obtained after aging for 100 h at 500 °C were investigated in both alloys by transmission electron microscopy (TEM) and scanning electron microscopy (SEM), using the same instruments and techniques described in Ref. [13].

A second set of alloys, Al–0.1Zr(c) and Al–0.1Zr–0.1Ti(c), were aged in a series of multi-step 3 h isochronal

aging steps beginning at 300 °C and terminating at 600 °C, in 25 °C increments. Between each aging step, the specimens were water-quenched and precipitation of Al_3Zr or $Al_3(Zr_{1-x}Ti_x)$ was monitored by Vickers microhardness and AC electrical conductivity measurements. The AC conductivity measurements were performed using an eddy current apparatus (Sigmatest 2.069 from Foerster Instruments, Pittsburgh, PA) at room temperature. Five measurements were recorded, each corresponding to a different frequency (60, 120, 240, 480, and 960 kHz) on each specimen. For consistency, a single specimen of each alloy was used for the AC electrical conductivity measurements, which was measured between each isochronal aging step. Finally, the microstructures obtained after isochronal aging to 450, 525, or 575 °C were investigated in both alloys by TEM.

3. Experimental results

3.1. Isothermal aging (500 °C)

Fig. 1 displays Vickers microhardness as a function of aging time at 500 °C for Al–0.1Zr(b) and Al–0.1Zr–0.1Ti(b) (after aging at 375 °C for 100 h). The hardness decreases linearly on a semi-logarithmic scale, from ca. 450 MPa in the peak-aged condition to ca. 265 MPa after a 400 h exposure at 500 °C. Both alloys overage at the same rate with no improved coarsening resistance of $Al_3(Zr_{1-x}Ti_x)$ ($L1_2$) as compared to Al_3Zr ($L1_2$). These results are consistent with those of our prior microstructural study [13], where the precipitate radii of Al_3Zr ($L1_2$) and $Al_3(Zr_{1-x}Ti_x)$ ($L1_2$) precipitates are identical, within experimental error, after extended aging times (1600 h) during isothermal aging at 425 °C.

Table 1
Compositions and aging conditions of the Al–Zr and Al–Zr–Ti alloys investigated

	Nominal concentration (at.%)		Verified concentration (at.%)		Aging temperatures (°C)
	Zr	Ti	Zr	Ti	
Al–0.1Zr(b)	0.1	–	0.085	–	500
Al–0.1Zr(c)	0.1	–	0.101	–	300–600 (isochronal)
Al–0.1Zr–0.1Ti(b)	0.1	0.1	0.089	0.099	500
Al–0.1Zr–0.1Ti(c)	0.1	0.1	0.095	0.091	300–600 (isochronal)
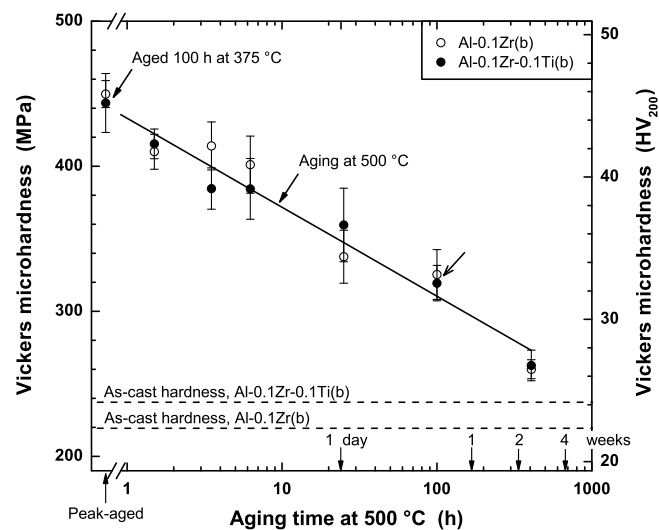
Fig. 1. Vickers microhardness vs. exposure time at 500 °C for Al–0.1Zr(b) and Al–0.1Zr–0.1Ti(b) alloys (after peak aging at 375 °C for 100 h). The rightmost arrow on the curve indicates exposure times investigated by conventional TEM.

The overaging behavior exhibited in Fig. 1 was investigated by TEM and SEM, and can be explained by dissolution of the small, high number density Al_3Zr ($L1_2$) or $Al_3(Zr_{1-x}Ti_x)$ ($L1_2$) precipitates within the dendritic cells that re-precipitate heterogeneously on grain boundaries, small-angle grain boundaries, or dislocations, ultimately forming extensive arrays of heterogeneously nucleated equilibrium $D0_{23}$-structured precipitates. Fig. 2 displays montages of complementary bright-field and dark-field TEM micrographs of Al–0.1Zr–0.1Ti(b) aged at 500 °C for 100 h (after aging at 375 °C for 100 h). Several dislocations are visible, on which numerous disk-shaped, ca. 150–200 nm diameter and 50 nm thick, equilibrium $D0_{23}$-structured precipitates have formed (precipitates A in Fig. 2). The dislocations and linear arrays of precipitates are most apparent in the bright-field TEM micrographs in Fig. 2. Arrays of spheroidal $L1_2$ precipitates, labeled B in Fig. 2, also appear to be heterogeneously nucleated along the same dislocation array as the equilibrium $D0_{23}$ precipitates described above. These precipitates are surrounded by a narrower (50–200 nm radius) precipitate-depleted zone, suggesting that the heterogeneously nucleated metastable $L1_2$ phase precedes formation of the disk-shaped $D0_{23}$ phase. The precipitates labeled C in Fig. 2 are other examples of transformation to the equilibrium $D0_{23}$ structure occurring heterogeneously on dislocations cutting through a precipitate-rich dendrite, leaving behind precipitate-depleted zones surrounding the dislocations. The precipitate-denuded zones labeled D arise from Ostwald ripening (coarsening) of slightly larger precipitates at the dendrite's periphery.

The arrays of heterogeneously nucleated $D0_{23}$ precipitates extend for hundreds of micrometers and are observable also by SEM, Fig. 3, which displays similar arrays of disk-shaped precipitates. For a metal at room temperature, the dislocation density is of the order of 10^{10} m^{-2} [14], or one dislocation per 10×10 μm^2 area. Thus, the area represented in Fig. 3a is expected to contain ca. 43 dislocations, intersecting the specimen at various orientations. It is conceivable that the long array of disk-shaped precipitates in
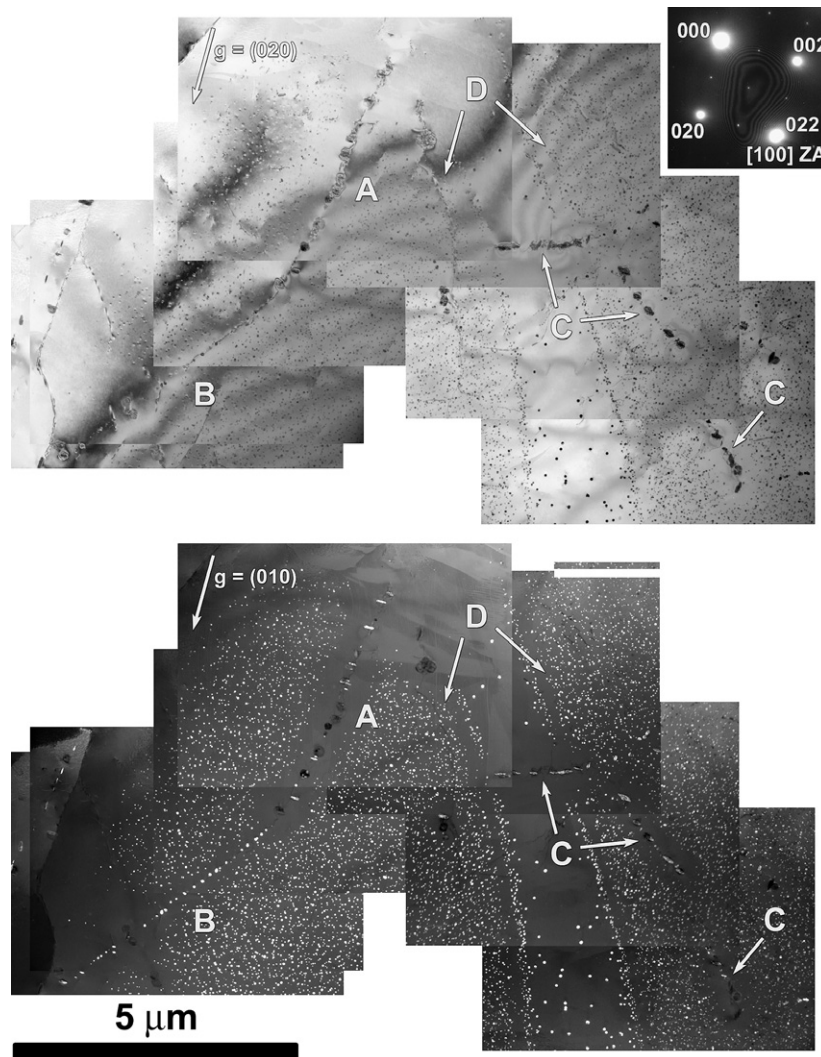
Fig. 2. Montage of bright-field (imaged with the $\vec{g} = (0\,2\,0)$ reflection) and dark-field (imaged with $\vec{g} = (0\,1\,0)$ $L1_2$ superlattice reflection). TEM micrographs of Al–0.1Zr–0.1Ti(b) aged at 500 °C for 100 h (after peak aging at 375 °C for 100 h).
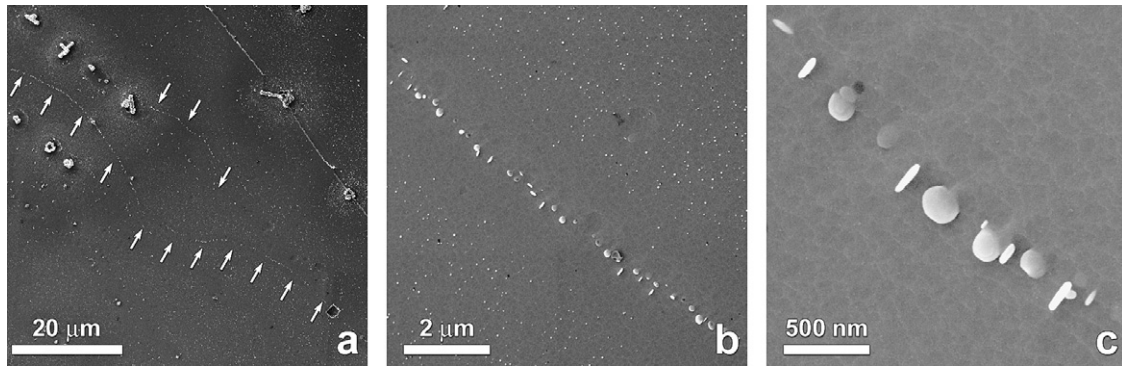
Fig. 3. SEM micrographs of Al$_3$Zr (D0$_{23}$) precipitates in Al–0.1Zr(b) aged at 500 °C for 100 h (after peak aging at 375 °C for 100 h). (a) Arrays of heterogeneously nucleated D0$_{23}$ precipitates extend for hundreds of micrometers, suggesting that they are nucleated on small-angle grain boundaries. (b) Precipitate-free zone extending 1.5 μm to either side of the heterogeneously nucleated array of D0$_{23}$ precipitates. (c) The morphology of the D0$_{23}$ phase is disk-shaped, 150–200 nm in diameter and 50–60 nm in thickness, and exhibits one of three possible orientation relationships with the α-Al solid solution.

Fig. 3 are nucleated on a single dislocation which, by chance, lies along the surface of the electropolished specimen viewed in SEM. A more likely scenario, however, is that the precipitates are nucleated on planar dislocation arrays associated with a small-angle grain boundary.

The disk-shaped D0$_{23}$ precipitates exist in one of three orientations: two orthogonal edge-on orientations and one face-on when viewed along $[100]_{\alpha\text{-Al}}$, indicating a cube-on-cube orientation relationship with the α-Al solid-solution matrix. If the arrays of D0$_{23}$ precipitates were heterogeneously nucleated on a single isolated dislocation, a preferred orientation relationship of the disk-shaped precipitates might be expected – the one that makes best use of the dislocation strain field to lower its net reversible work of formation. Figs. 2 and 3 indicate, however, that all three orientations are observed along a given linear feature, further suggesting that heterogeneous nucleation is occurring on a dislocation network associated with a small-angle grain boundary.

The equilibrium precipitates appear to be at least partially coherent with α-Al, as evidenced by strong strain-field contrast when imaged under two-beam conditions in bright-field TEM, Fig. 4a. Because of their large size (ca. 200 nm in diameter), the disk-shaped precipitates are most likely semi-coherent with the α-Al matrix, which

is also supported by the appearance of striped lines of contrast normal to $\vec{g}$ in the images of many of the precipitates when viewed face-on in Fig. 4c. These are interpreted as contrast effects due to interfacial dislocations, indicating semi-coherency with the α-Al matrix. Depending on their orientation, only certain disk-shaped precipitates are illuminated in dark-field TEM. In Fig. 4b, those precipitates viewed face-on along $[100]_{\alpha\text{-Al}}$ appear dark when imaged with $\vec{g} = (010)$. Using $\vec{g} = (011)$, as in Fig. 4d, the same orientation appears bright. This indicates that the precipitates have the D0$_{23}$ structure, as discussed in Section 4.1.

Within the precipitate-rich dendrites, Fig. 5, the spheroidal precipitates have the metastable L1$_2$ structure, are coherent with the α-Al solid solution, and exhibit excellent coarsening resistance after aging at 500 °C for 100 h (preceded by aging at 375 °C for 100 h). The mean radii of these Al$_3$Zr and Al$_3$(Zr$_{1-x}$Ti$_x$) precipitates, Fig. 5a and c, are statistically identical: 12.3 ± 2.9 nm (based on 206 precipitates) and 12.0 ± 4.0 nm (based on 168 precipitates), respectively, which is consistent also with the identical decrease in hardness exhibited by both alloys during exposure at 500 °C in Fig. 1.
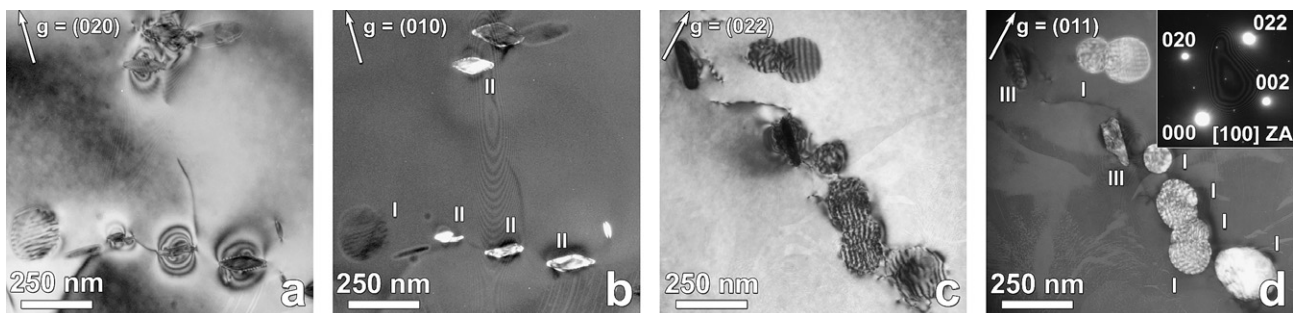
Fig. 4. Complementary bright-field and dark-field conventional TEM micrographs of heterogeneously nucleated D0$_{23}$ precipitates on dislocations in Al–0.1Zr–0.1Ti(b) aged at 500 °C for 100 h (after peak aging at 375 °C for 100 h). The strong contrast and presence of interfacial dislocations in bright-field indicates that the disk-shaped precipitates are semi-coherent with the α-Al matrix. In dark-field, only certain orientations are illuminated, depending on the $\vec{g}$ vector that is operating.
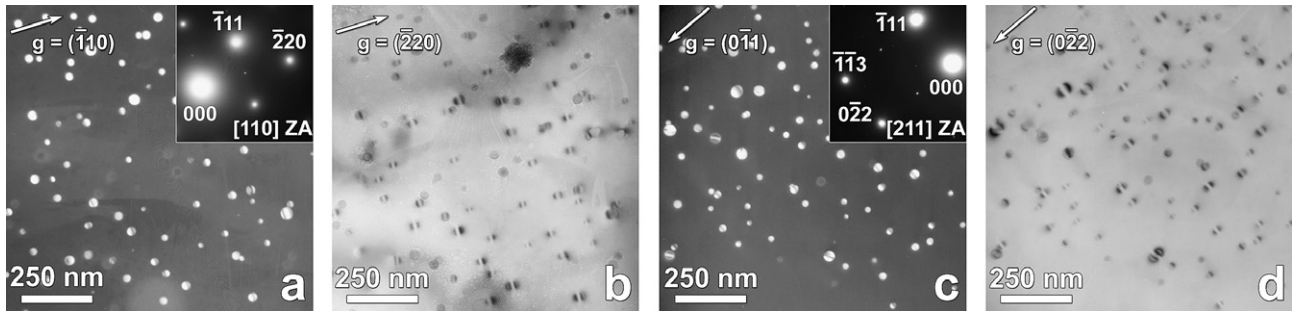
Fig. 5. Complementary dark-field and bright-field TEM micrographs of intradendritic precipitates in Al–0.1Zr(b) (panels a and b) and Al–0.1Zr–0.1Ti(b) (panels c and d) aged at 500 °C for 100 h (after peak aging at 375 °C for 100 h). The Al_3Zr or $Al_3(Zr_{1-x}Ti_x)$ precipitates have the metastable $L1_2$ structure and are coherent with the α-Al solid-solution matrix, with a mean radius, $\langle R \rangle$, of ca. 12 nm.

3.2. Isochronal aging (300–600 °C)

Fig. 6 indicates the precipitation behavior of Al–0.1Zr(c) and Al–0.1Zr–0.1Ti(c) during isochronal aging steps, as
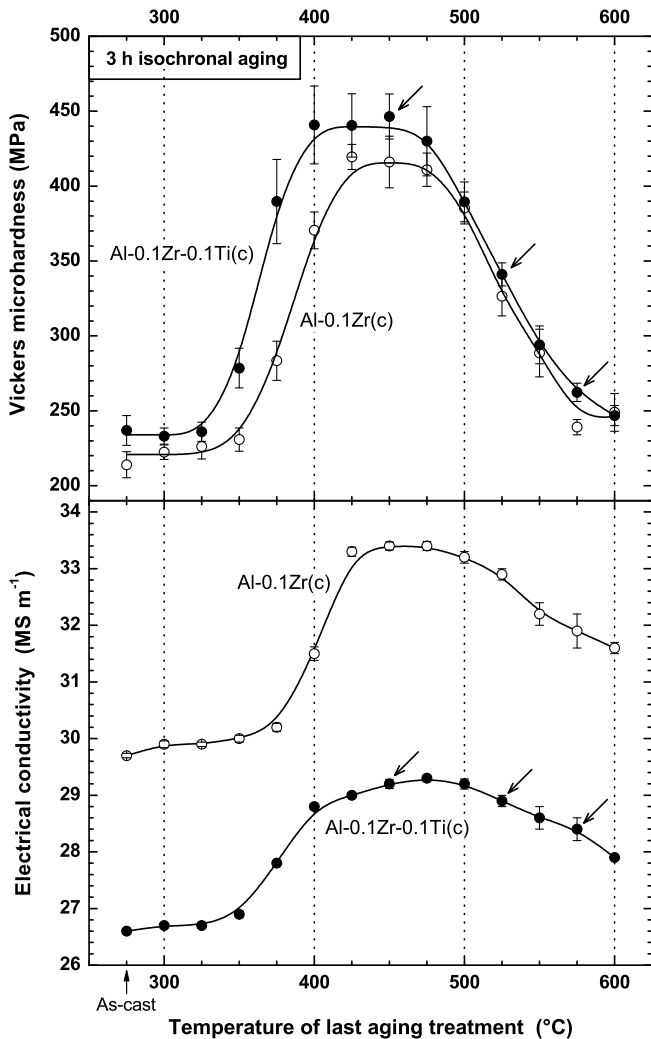
Fig. 6. Vickers microhardness and AC electrical conductivity evolution during isochronal aging (3 h at each temperature) of Al–0.1Zr(c) and Al–0.1Zr–0.1Ti(c). The arrows on the curves for Al–0.1Zr–0.1Ti(c) indicate aging times investigated by conventional TEM, shown in Fig. 7.

monitored by Vickers microhardness and AC electrical conductivity measurements. Precipitation of Al_3Zr ($L1_2$) commences between 350 and 375 °C in the binary alloy, as evidenced by the increase in strength and the accompanying change in AC electrical conductivity. For the ternary alloy, precipitation of $Al_3(Zr_{1-x}Ti_x)$ ($L1_2$) commences at temperatures lower by about 25 °C, consistent with the accelerated isothermal nucleation kinetics (shorter incubation time) for Al–0.1Zr–0.1Ti(b) as compared with Al–0.1Zr(b) observed during isothermal aging [13]. The maximum hardness achieved during isochronal aging is also slightly greater (by ca. 25 MPa) in the Ti-containing alloy, indicating a finer size, and/or larger volume fraction, of $Al_3(Zr_{1-x}Ti_x)$ ($L1_2$) precipitates. The latter possibility seems more likely since, as discussed below, the measured precipitate radii in both alloys are equivalent for a given aging treatment.

Beyond 475 °C, rapid overaging (as evidenced by a continuous decrease in microhardness) is accompanied by a similar decline in electrical conductivity for both Al–0.1Zr(c) and Al–0.1Zr–0.1Ti(c). As discussed below, the overaging observed in Fig. 6 is due to coarsening and dissolution of the spheroidal $L1_2$-structured Al_3Zr or $Al_3(Zr_{1-x}Ti_x)$ precipitates, and their transformation to their respective equilibrium $D0_{23}$ structures. Precipitate dissolution, controlled by the temperature dependence of the solid solubility of Zr and/or Ti in α-Al, explains the decrease in AC conductivity for $T > 475$ °C observed in Fig. 6.

Microstructural coarsening of the alloys, which occurs for $T > 450$ °C (Fig. 6), was investigated directly by TEM in both alloys after isochronal aging steps to 450, 525, or 575 °C. Fig. 7a and b displays the microstructure in Al–0.1Zr–0.1Ti(c) isochronally aged to 450 °C, which corresponds to the early stages of coarsening, Fig. 6. Distinct, well-defined, precipitate-rich dendrites are observed. All precipitates have a spheroidal morphology with the metastable $L1_2$ structure. Within the dendrites, Fig. 7a, there is evidence of precipitate coalescence occurring on dislocations (indicated by arrows), representing the early stages of microstructural coarsening. The spheroidal intradendritic precipitates have a mean radius $\langle R \rangle = 3.4 \pm 0.5$ nm, Fig. 7b.
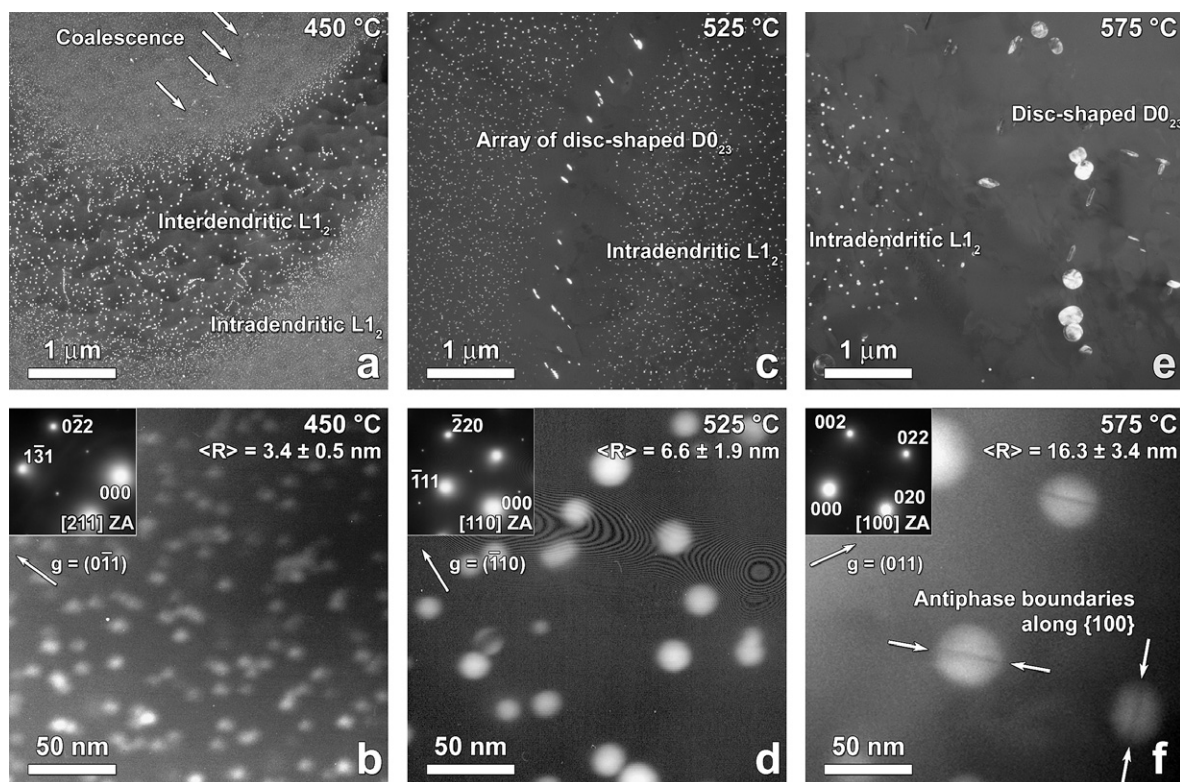
Fig. 7. Centered superlattice dark-field TEM micrographs of Al–0.1Zr–0.1Ti(c) isochronally aged to 450, 525, or 575 °C.

Fig. 7c and d shows the microstructure in Al–0.1Zr–0.1Ti(c) isochronally aged to 525 °C, which corresponds to an intermediate stage of coarsening in Fig. 6. Fig. 7c displays disk-shaped $D0_{23}$ precipitates heterogeneously nucleated on a dislocation cutting through a precipitate-rich dendrite. A surrounding precipitate-free zone, up to 800 nm in width, is formed as a result of the $D0_{23}$ formation, similar to that described previously in Figs. 2 and 3 during isothermal aging at 500 °C. Within the dendrites, most precipitates are spheroidal and have the $L1_2$ structure, with a mean radius $\langle R \rangle = 6.6 \pm 1.9$ nm, Fig. 7d.

After reaching 575 °C, most of the precipitates are transformed to the disk-shaped $D0_{23}$ structure, as demonstrated in Fig. 7e. The disk-shaped equilibrium precipitates exhibit a cube-on-cube orientation relationship with α-Al, as discussed for Figs. 2 and 3. There are, nevertheless, other regions (presumably remnants of the initial precipitate-rich dendrites) containing spheroidal $L1_2$ precipitates, which have a mean radius $\langle R \rangle = 16.3 \pm 3.4$ nm, Fig. 7f.

The TEM micrographs in Fig. 7 are for Al–0.1Zr–0.1Ti(c) but are representative of the binary Al–0.1Zr(c) as well. Indeed, Table 2 demonstrates that measured precipitate radii in Al–0.1Zr(c) and Al–0.1Zr–0.1Ti(c) after isochronal aging to the same temperatures (450, 525, or 575 °C) are statistically identical, consistent with their similar overaging behavior demonstrated in Fig. 6.

Fig. 8 displays complementary dark-field and bright-field TEM micrographs of intradendritic $L1_2$ precipitates in Al–0.1Zr(c) and Al–0.1Zr–0.1Ti(c) isochronally aged

Table 2
Mean precipitate radii, $\langle R \rangle$, of intradendritic precipitates in Al–0.1Zr(c) and Al–0.1Zr–0.1Ti(c) isochronally aged to 450, 525, and 575 °C

Alloy	Last aging treatment (°C)	Mean precipitate radius, $\langle R \rangle$ (nm)	Number of precipitates counted
Al–0.1Zr(c)	450	3.7 ± 0.5	188
	525	6.8 ± 1.8	180
	575	16.9 ± 4.4	75
Al–0.1Zr–0.1Ti(c)	450	3.4 ± 0.5	99
	525	6.6 ± 1.9	205
	575	16.3 ± 3.4	85

to 575 °C. As discussed, the precipitates have the same mean radius, 16.9 ± 4.4 nm and 16.3 ± 3.4 nm, respectively (Table 2). Moreover, they are coherent with α-Al as demonstrated by the Ashby–Brown strain-field contrast exhibited in the bright-field TEM micrographs in Fig. 8. Considering the size of these precipitates, their coherency is not surprising since their radii are below the ca. 35 nm radius threshold for coherency loss discussed in our prior study [13].

4. Discussion

4.1. Structure and diffraction contrast of the $D0_{23}$ precipitates

Fig. 9 displays kinematically simulated [15] diffraction patterns of the metastable cubic $L1_2$ and equilibrium
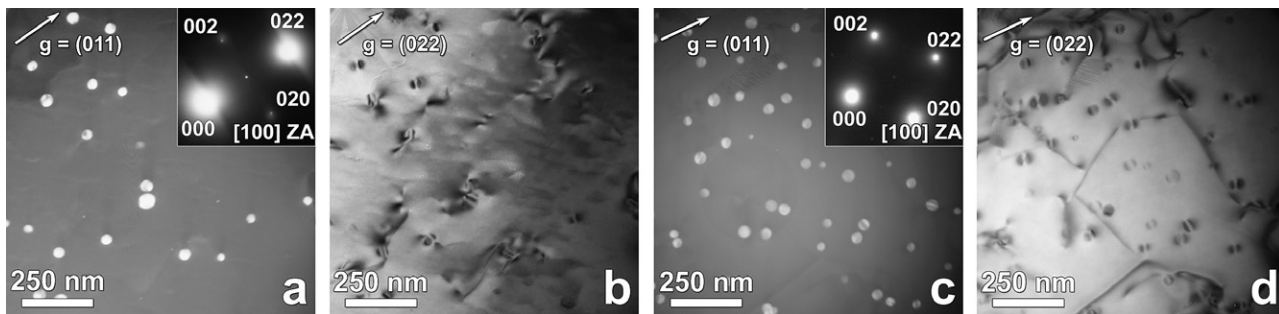
Fig. 8. Complementary dark-field and bright-field conventional TEM micrographs of precipitates in the precipitate-rich dendritic regions of Al–0.1Zr(c) (panels a and b) and Al–0.1Zr–0.1Ti(c) (panels c and d) isochronally aged to 575 °C. The Al_3Zr or $Al_3(Zr_{1-x}Ti_x)$ precipitates have the metastable $L1_2$ structure and are coherent with the α-Al solid-solution matrix, with a mean radius, $\langle R \rangle$, of ca. 16.5 nm.

tetragonal $D0_{23}$ Al_3Zr phases in the three possible cube-on-cube orientations with α-Al (denoted as orientations I, II, or III), when viewed along $[100]_{\alpha\text{-Al}}$. The simulated diffraction patterns for the equilibrium $D0_{23}$ structure agree with the experimental selected area diffraction patterns (SADPs) displayed in Fig. 10, indicating that the disk-shaped precipitates have the equilibrium $D0_{23}$ structure of Al_3Zr. The c-axis of the $D0_{23}$ unit cell is aligned along the axis of the disk, reflecting the tetragonal $D0_{23}$ symmetry. The lattice parameters of Al_3Zr $(D0_{23})$ are $a = b = 0.4014$ and $c = 1.7321$ nm, resulting in lattice-parameter mismatches with α-Al $(a = 0.40496$ nm) of $\delta_a = \delta_b = -0.88\%$ and $\delta_c = 6.92\%$ at room temperature [1]. Since the lattice parameter mismatch is the largest in the c-direction, precipitates that are thin in this dimension are preferred, explaining the disk morphology. The relatively large mismatch with α-Al also explains why the equilibrium phase is only observed when heterogeneously nucleated along dislocations.

4.2. Transformation mechanism to the equilibrium $D0_{23}$ structure

The precipitates with the equilibrium $D0_{23}$ structure are not nucleated directly from the supersaturated α-Al solid solution during aging, but rather form by dissolution and subsequent re-precipitation of solutes from nearby pre-existing $L1_2$ precipitates (formed either during the prior isothermal aging treatment at 375 °C [13], or during earlier isochronal aging steps, Section 3.2). The consumption of the pre-existing $L1_2$ precipitates is shown unambiguously in the bottom-most precipitate-rich dendrite in each of the montages in Fig. 2, which initially contained a relatively large number density of homogeneously distributed spheroidal $L1_2$ $Al_3(Zr_{1-x}Ti_x)$ precipitates in the peak-aged condition (isothermally aged 100 h at 375 °C). During aging at 500 °C, the equilibrium $D0_{23}$ precipitates form heterogeneously along a dislocation cutting through the dendrite, leaving behind a precipitate-free zone approximately 1 μm in width around the dislocation (precipitates A in Fig. 2). A similar precipitate-free zone extends 1.5 μm to either side of the heterogeneously nucleated array of disk-shaped Al_3Zr precipitates in Fig. 3b. The

widths of these precipitate-free zones are comparable to the calculated root-mean-square (RMS) diffusion distance, $\sqrt{4Dt}$ (using values $Q = 242$ and 260 kJ mol^{-1} and $D_0 = 7.28 \times 10^{-2}$ and 1.12×10^{-1} m^2 s^{-1} for Zr and Ti, respectively [1]), of Zr or Ti after 100 h at 500 °C, which is 2.2 or 0.66 μm, respectively. Similar arrays of heterogeneously nucleated $D0_{23}$ precipitates cutting through precipitate-rich dendrites are observed in Fig. 7c after isochronal aging to 525 °C. In this case the calculated cumulative RMS diffusion distance of Zr or Ti atoms is 1.4 or 0.44 μm, respectively, which is comparable to the radius of the precipitate-free cylinder visible in Fig. 7c.

During the latter stages of coarsening, the spheroidal $L1_2$ precipitates develop structural faults, characterized by sharp lines of no-contrast parallel to {100}-type planes inside the precipitates, as displayed in Fig. 7f for Al–0.1Zr–0.1Ti(c) isochronally aged to 575 °C. Zedalis and Fine [7] observed similar faults in Al_3Zr $(L1_2)$ precipitates formed after aging Al–0.22Zr (at.%) at 600 °C for 12 h, which they postulated to be antiphase boundaries (APBs). This was confirmed by Chen et al. [11,16] studying $Al_3(Zr_{1-x}V_x)$ $(L1_2)$ precipitates formed in melt-spun Al–0.34Zr–0.98 V (at.%) alloys aged at 500 °C. Using high resolution electron microscopy, the latter researchers showed that the APBs are associated with a displacement of $a/2\langle 110 \rangle$ on {100} planes [16]. Lee et al. [17] detected similar planar faults in $L1_2$ precipitates formed in Al–0.8Zr–0.8V–0.4Ti (at.%) alloys aged at 425 °C for 200–400 h. Ryum [18] demonstrated that the transformation from the cubic $L1_2$ structure to an imperfect tetragonal structure involves the introduction of an APB with a displacement vector $a/2\langle 110 \rangle$ on {100}-type planes in $D0_{22}$-structured Al_3Hf. The observed APBs in the spheroidal $L1_2$-structured precipitates (Fig. 7f) therefore represent the early stages of the transformation to the equilibrium $D0_{23}$ structure.

The APBs generated in the transition to an imperfect $D0_{23}$ structure are even more pronounced in the heterogeneously nucleated and (because of pipe diffusion) faster-growing interdendritic $L1_2$ precipitates. Fig. 11a and b are complementary bright-field and dark-field TEM micrographs displaying heterogeneously nucleated $Al_3(Zr_{1-x}, Ti_x)$ precipitates in Al–0.1Zr–0.1Ti(b) aged at 500 °C for 100 h (after aging at 375 °C for 100 h), in which the APBs
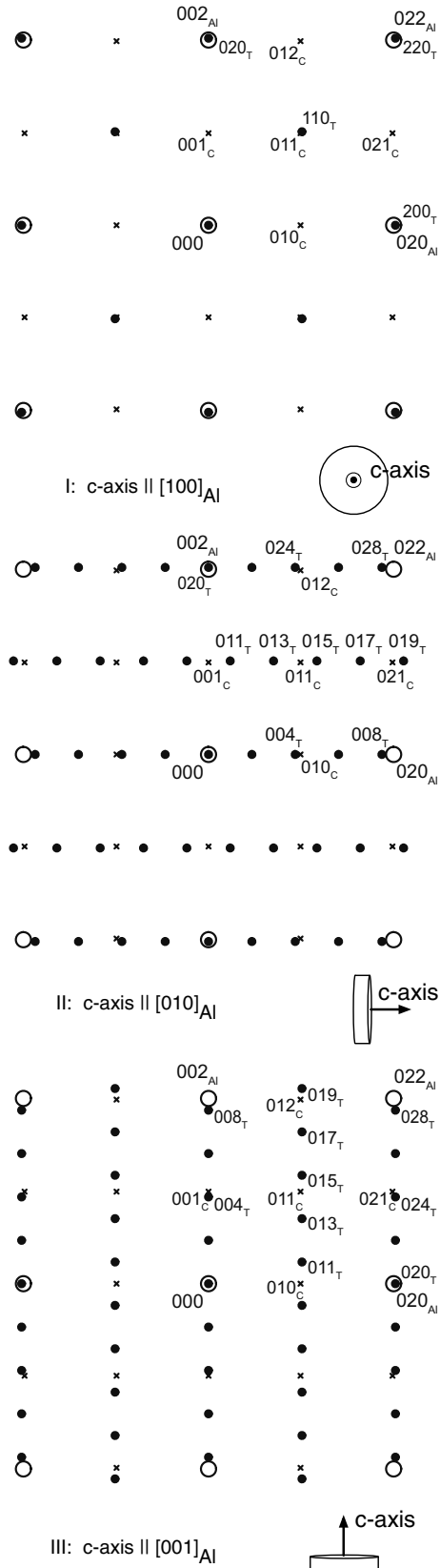
Fig. 9. Kinematically simulated [15] electron diffraction patterns of the metastable cubic L1$_2$ (crosses, C subscript) and equilibrium tetragonal D0$_{23}$ (closed circles, T subscript) Al$_3$Zr phases in the three possible orientation relationships with α-Al (open circles), viewed along [1 0 0]$_{α\text{-Al}}$. The spots not indexed (e.g., 0 0 2$_T$, 0 0 6$_T$) are kinematically forbidden.

are especially prevalent. The larger heterogeneously nucleated precipitates exhibit preferential growth in ⟨1 0 0⟩ directions, along the APB, forming elongated ellipsoidal morphologies, consistent with prior observations [7,11,17]. This is believed to be a transition morphology between the spheroidal metastable L1$_2$ phase and the disk-shaped equilibrium D0$_{23}$ phase. Fig. 11c shows other examples of elongated precipitates containing APBs nucleated on several dislocations. Note that both the APBs and the precipitates' major axis lie along ⟨1 0 0⟩-type crystallographic directions and do not align themselves along the dislocation.

4.3. Other precipitate morphologies

Not all of the D0$_{23}$-structured precipitates exhibit the disk-shaped morphology described in Section 4.1; Figs. 4a and 11c, for example, display equilibrium Al$_3$(Zr$_{1-x}$Ti$_x$) precipitates with a rhombohedral morphology. When precipitation of D0$_{23}$ from α-Al solid solution occurs in the manner described above (cube-on-cube with α-Al), the principal axes of the tetragonal unit cell (point group 4/mmm, order 16) are parallel to those of the α-Al matrix (point group m3m, order 48), and the intersection point group [19], defined by the symmetry elements preserved during transformation, is thus 4/mmm and of order 16. Symmetry thus requires there be 48/16 or 3 variants of the precipitate phase as in Fig. 9. If, however, the equilibrium tetragonal D0$_{23}$ phase is nucleated such that the a-, b-, and c-axes are not parallel to the α-Al matrix, the intersection point group loses all symmetry elements except for the common center of inversion, which possibly explains the rhombohedral morphology observed in Figs. 4a and 11c. It is also possible that this morphology is a result of kinetics, perhaps related to anomalous growth by pipe diffusion because these precipitates are nucleated on dislocations. It is further possible that these rhombohedral-shaped precipitates do not have the equilibrium D0$_{23}$ structure. More detailed analytical TEM is necessary to sort out these possibilities.

4.4. Temperature of the L1$_2$ → D0$_{23}$ transformation

The L1$_2$ → D0$_{23}$ structural transformation occurs at approximately 500 °C, which corresponds also to the onset of significant overaging as observed by Vickers microhardness in Figs. 1 and 6. During isothermal aging of Al–0.1Zr and Al–0.1Zr–0.1Ti at 425 °C (0.75T_m), equilibrium D0$_{23}$ precipitates are not observed [13]. In the present isochronally-aged alloys, D0$_{23}$ precipitates are not observed at 450 °C, Fig. 7a, and are observed only to a limited extent at 525 °C, Fig. 7c. After extended aging times (100 h) at 500 °C, Figs. 2 and 3, the transformation is extensive along dislocations, although most precipitates still have the metastable L1$_2$ structure. Even at 575 °C L1$_2$ precipitates are observed, Fig. 7e and f, indicating that the L1$_2$ → D0$_{23}$ transformation does not occur equally throughout the
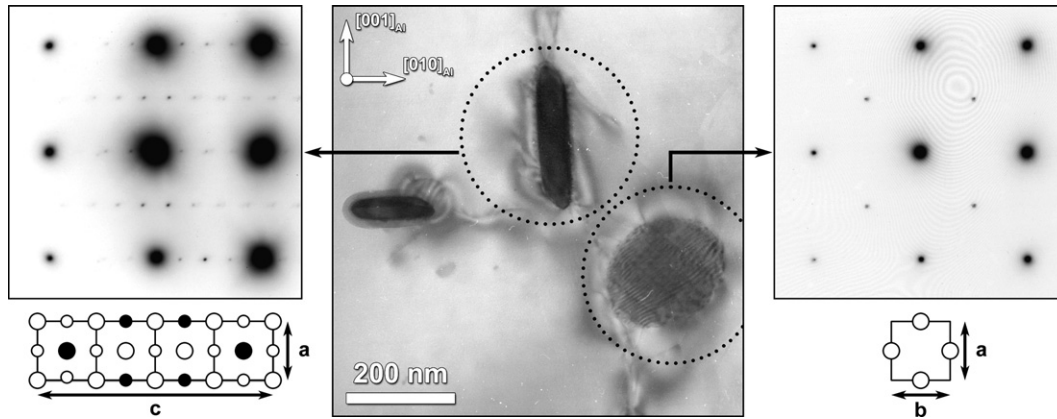
Fig. 10. Bright-field TEM micrograph of disk-shaped $D0_{23}$ precipitates in three possible orientations and corresponding selected area diffraction patterns (SADPs) of the equilibrium $D0_{23}$ phase in Al–0.1Zr–0.1Ti(b) aged at 500 °C for 100 h (after aging at 375 °C for 100 h). The patterns are indexed in Fig. 9.
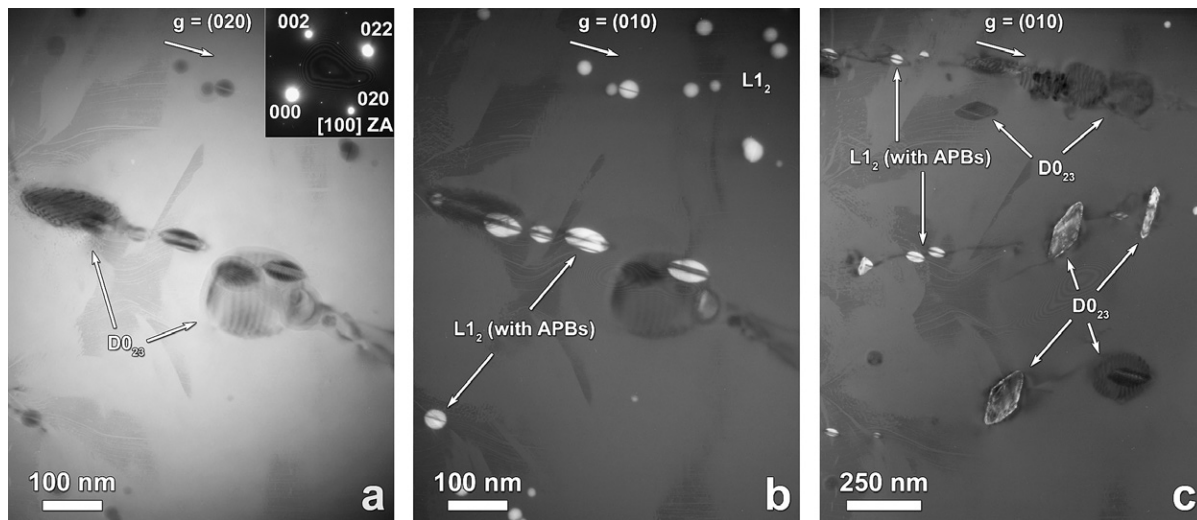
Fig. 11. TEM micrographs of heterogeneously nucleated $D0_{23}$ precipitates on dislocations in Al–0.1Zr–0.1Ti(b) aged at 500 °C for 100 h (after aging at 375 °C for 100 h). Many of the precipitates with the $L1_2$ structure exhibit antiphase boundaries (APBs) parallel to {100}, indicating the transformation to the equilibrium $D0_{23}$ structure.

alloy. This is further illustrated in Fig. 11, which displays spheroidal $L1_2$ precipitates, partially transformed imperfect $L1_2$ precipitates with APBs, and disk-shaped $D0_{23}$ precipitates in close proximity. Additional factors, including aging time and dislocation density in the specimen, also influence the kinetics and the apparent transformation temperature. Nevertheless, the structural transformation process seems to occur at 500 °C within technologically reasonable aging times.

This conclusion concurs with results of several studies in the scientific literature. Zedalis and Fine [7] observed transformation to the equilibrium $D0_{23}$ structure in Al–0.24Zr (at.%) aged at 450 °C. Their specimens, however, were initially cold rolled 95%; the high dislocation density therefore explains why these researchers observed $D0_{23}$ precipitates at a relatively low aging temperature. Izumi and Oelschlägel [20] reported $L1_2$-structured Al_3Zr precipitates in an Al–0.33Zr (at.%) aged at 450 °C, which, after extended aging times (218 h), had not transformed to the

stable $D0_{23}$ structure; the $L1_2$ precipitates were resistant to coarsening with $\langle R \rangle = 10.9$ nm. Nes [21] aged an Al–0.05Zr (at.%) alloy at 460 °C for upwards of 700 h and observed small, $\langle R \rangle = 35$ nm Al_3Zr ($L1_2$) precipitates, and, like Izumi and Oelschlägel [20], never observed the equilibrium $D0_{23}$ structure at this temperature. Ryum [22] studied precipitation of Al_3Zr ($L1_2$) in a chill-cast Al–0.15Zr (at.%) alloy aged at 500 °C; the equilibrium $D0_{23}$ structure was observed only after long aging times (>120 h), primarily at grain boundaries. Dahl et al. [23], investigating several Al–Zr alloys containing 0.03–0.36 at.% Zr aged at 200–500 °C, similarly concluded that the $L1_2 \rightarrow D0_{23}$ structural transformation begins after several hundred hours at 500 °C. Finally, Srinivasan et al. [24] produced single-phase Al_3Zr ($L1_2$) specimens through mechanical alloying of pure elemental powders, and found that the $L1_2 \rightarrow D0_{23}$ transformation occurs at 550 °C, as monitored by X-ray diffraction and differential scanning calorimetry.

4.5. Mechanisms of microstructural coarsening

The mechanism of microstructural coarsening described in this study is summarized schematically in Fig. 12, in which four stages of coarsening are defined. Stage I coarsening corresponds to the peak-aged condition, where well-defined, precipitate-rich dendrites contain a dense distribution of small ($\langle R \rangle$ <5 nm) coherent $L1_2$ precipitates. Larger interdendritic spheroidal $L1_2$ precipitates, which are discussed in our prior microstructural study [13], are also depicted in Fig. 12, many of them heterogeneously nucleated on dislocations.

Stage II is the initiation of microstructural coarsening, where intradendritic $L1_2$ precipitates coarsen by Ostwald ripening and the heterogeneously nucleated interdendritic precipitates coarsen rapidly by dislocation pipe diffusion. Within the precipitate-rich dendrites, preferential coarsening occurs heterogeneously on dislocations, as shown in Fig. 7a. Stage II coarsening thus occurs at ca. 450 °C during isochronal aging, or after extended aging times (10^3 h) at 425 °C. A decrease in hardness is observed during this stage.

Stage III coarsening signals the beginning of the $L1_2 \rightarrow D0_{23}$ structural transformation, limited to dislocations and probably other heterogeneous nucleation sites such as grain boundaries. The heterogeneously nucleated $L1_2$ precipitates grow into elongated ellipsoidal-shaped precipitates, exhibiting preferential growth in $\langle 100 \rangle$ directions. APBs, characterized by sharp lines of no-contrast parallel to {100} planes inside the $L1_2$ precipitates, indicate the onset of the transition to the $D0_{23}$ structure. The transformation to the disk-shaped $D0_{23}$ phase occurs at the expense of the surrounding $L1_2$ precipitates, resulting in precipitate-free cylinders up to ca. 1 µm in diameter surrounding the dislocations. This mechanism of coarsening is active by aging isochronally to 525 °C, Fig. 7c.

By Stage IV coarsening, most of the metastable $L1_2$ precipitates have transformed to the equilibrium $D0_{23}$ structure. There are, however, remnants of the precipitate-rich dendrites that still contain coherent, spheroidal $L1_2$ precipitates that have further coarsened. Despite their presence, however, virtually all hardness is lost on the macroscopic scale.
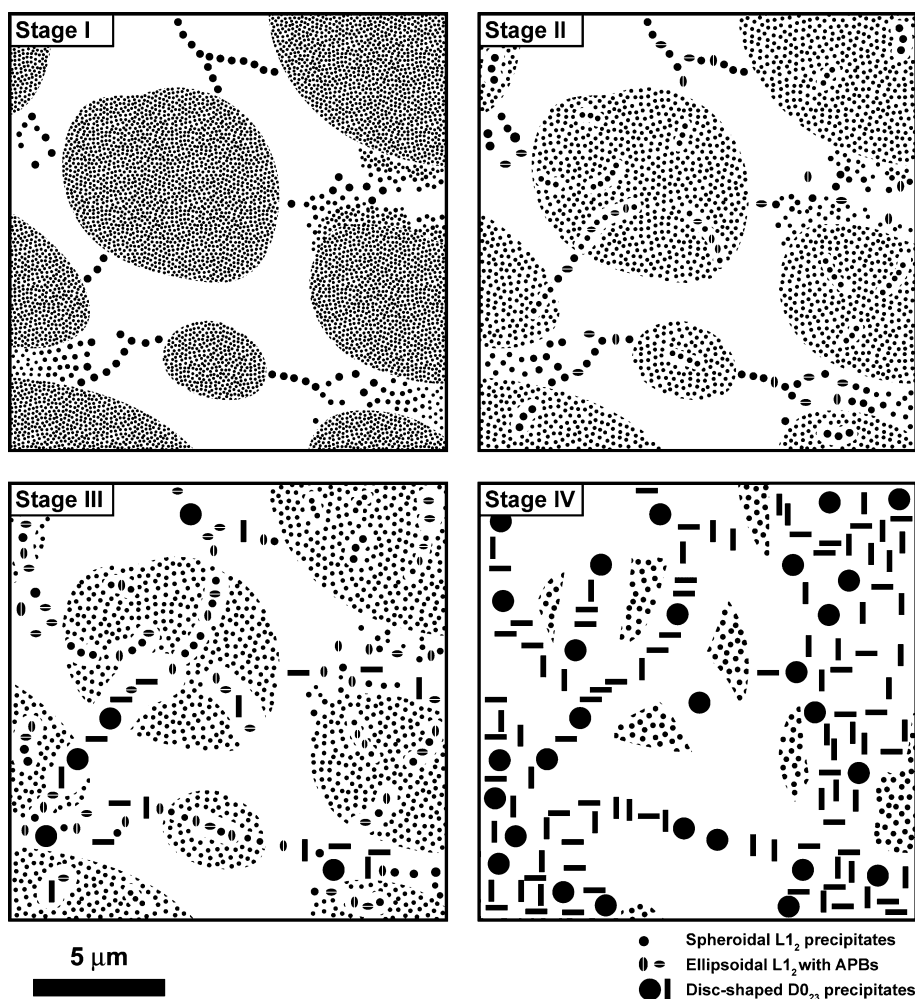
Fig. 12. Schematic of four stages of microstructural coarsening occurring on the nanometer-scale of the precipitates and the micrometer-scale of the dendrites. A representative scale bar for the dendritic regions is indicated. Precipitates are not drawn to scale.

4.6. Mechanism of strengthening

In the absence of other strengthening mechanisms, precipitate shearing, precipitate bypass by dislocation looping, or a combination of these two mechanisms can generally explain ambient temperature strength in coarse-grained, non-strain-hardened, precipitate-strengthened alloys [25–27]. For large precipitate radii, R, the strength is controlled by Orowan dislocation looping, given by:

$$\Delta\sigma_{\text{or}} = M \cdot \frac{0.4 \cdot Gb}{\pi\sqrt{(1-v)}} \cdot \frac{\ln\left(\frac{2\bar{R}}{b}\right)}{\lambda_{e-e}} \qquad (1)$$

where $M = 3.06$ [28], $b = 0.286$ nm [29], $G = 25.4$ GPa [29], and $v = 0.345$ [28] for Al. For a monodispersed population of precipitates, the mean planar radius is $\bar{R} = \frac{\pi}{4}\langle R \rangle$, and the edge-to-edge inter-precipitate distance is $\lambda_{e-e} = \left(\sqrt{\frac{2\pi}{3\phi}} - \frac{\pi}{2}\right)\langle R \rangle$, where ϕ is the precipitate volume fraction [26,27,30]; these expressions are also good approximations for polydispersed arrays [27]. Deformation by dislocation shearing is expected to occur at small R, and calculations for these shearing mechanisms are applicable only for $R < 3$ nm [31], confirming that the Orowan bypass mechanism is operative for the values of $\langle R \rangle$ measured in Table 2. This is consistent also with prior studies on Al–Sc [32], Al–Sc–Zr [33], Al–Mg–Sc [34], Al–Sc–Ti [35] and Al–Sc–RE (RE, rare earth) [36] alloys with shearable, coherent Al$_3$Sc (L1$_2$) precipitates, where the Orowan bypass mechanism, Eq. (1), accurately predicts strengthening.

For a homogeneous alloy containing 0.1 at.% Zr, the equilibrium volume fraction of precipitated Al$_3$Zr is $\phi = 0.004$ using the lever rule, assuming negligible solubility at the aging temperature. The solutes in the present alloys are microsegregated, however, with the dendrite centers enriched approximately twofold in Zr, as determined previously by energy-dispersive X-ray spectroscopy [13]. The equilibrium volume fraction of Al$_3$Zr precipitates in the dendrites is therefore about $\phi = 0.008$. Moreover, a small amount of Ti is incorporated into the precipitates, as measured in a prior study on similar alloys employing atom-probe tomography [37], and Ti also influences the metastable Al–Zr solvus, see below. While these effects are small, as evidenced by the isothermal age-hardening curves of Al–0.1Zr and Al–0.1Zr–0.1Ti, where Ti has little effect on the hardness [13], ternary additions will nevertheless influence ϕ.

As a point of reference, a value of $\phi = 0.004$ is assumed, which is approximately the total volume fraction (including precipitate-free regions) of Al$_3$Zr or Al$_3$(Zr$_{1-x}$Ti$_x$) precipitates in the alloy at peak strength. From the measured precipitate radii in Table 2 for alloys isochronally aged to 450 °C (peak strength), Eq. (1) predicts $\Delta\sigma_{\text{or}} = 134 \pm 12$ MPa for Al–0.1Zr(c) and $\Delta\sigma_{\text{or}} = 141 \pm 14$ MPa for Al–0.1Zr–0.1Ti(c). The observed increased strength in Fig. 6 (as compared to the value of the as-cast, unaged specimens and using a conversion factor of 3 between Vickers microhardness and strength [38]) is 67 ± 6 MPa for Al–

0.1Zr(c) and 70 ± 6 MPa for Al–0.1Zr–0.1Ti(c), which is a factor of two less than the predicted $\Delta\sigma_{\text{or}}$. This indicates that the observed strengthening, while probably controlled by the Orowan bypass mechanism, cannot be predicted by the measured value of $\langle R \rangle$, Eq. (1), which assumes a spatially uniform precipitate distribution. Precipitation strengthening in the segregated alloys must be occurring on multiple length scales, as expected from the nanometer-scale of the precipitates and the micrometer-scale of the precipitate-rich dendrites.

This is also illustrated by the data in Table 3, which compares experimentally measured precipitate radii and Vickers microhardness from Al–0.1Zr and Al–0.1Zr–0.1Ti alloys measured in this study and in a prior investigation during isothermal aging at 375–425 °C [13]. Specimens aged isochronally to 525 °C exhibit smaller radii ($\langle R \rangle = 7$ nm) than those aged isothermally at 425 °C ($\langle R \rangle = 11$ nm) or in a sequential 375 °C + 500 °C aging treatment ($\langle R \rangle = 12$ nm), despite having similar strengths. Thus, there is not a simple direct correlation between the measured $\langle R \rangle$ and strength, as Eq. (1) predicts.

4.7. Effect of aging temperature

Table 3 also demonstrates that thermal history has a strong influence on alloy strength. Increasing the aging temperature (decreasing the supersaturation) in any precipitation reaction reduces the chemical driving force for nucleation leading to: (i) larger precipitates (because the critical radius for nucleation is larger); and (ii) a reduced equilibrium volume fraction of precipitates. Higher aging temperatures lead consequently to reduced precipitation hardening, as observed in our prior study of Al–Zr and Al–Zr–Ti alloys isothermally aged at 375–425 °C [13].

The effect of aging temperature must also be interpreted within the context of the micrometer-scale dendritic distribution of Al$_3$Zr or Al$_3$(Zr$_{1-x}$Ti$_x$) precipitates. In peritectic Al–Zr or Al–Zr–Ti alloys, the cores of the dendritic cells are solute-enriched compared to those regions at the dendrite peripheries [13]. At higher aging temperatures (where the overall solute supersaturation is smaller), a smaller fraction of the cored dendritic α-Al solid solution nucleates precipitates. Higher aging temperatures, therefore, not only result in smaller volume fractions of the precipitated phase (true for any precipitation reaction), but because of the dendritic distribution of solutes, the volume fraction of dendrites rich in precipitates is also reduced.

This explains why, during isochronal aging (Fig. 6), hardness values of the order of 415 MPa may be obtained for Al–0.1Zr after aging up to 450 °C, whereas during isothermal aging at 425 °C, the attainable strength is much less: ca. 300 MPa [13]. A similar effect was observed by Sato et al. [39] during aging of an Al–0.17Zr (at.%) alloy at 450 °C, whereby linear heating at a controlled rate of 100 °C h^{-1} produced a nearly 200 MPa increase in peak hardness compared to the same alloy aged directly at 450 °C (540 MPa vs. 350 MPa).

Table 3
Mean precipitate radii, $\langle R \rangle$, observed in the dendritic cells after different thermal histories

	Aging treatment	Vickers microhardness (MPa)	Mean precipitate radius, $\langle R \rangle$ (nm)
Al–0.1Zr(b)	Isothermally aged at 425 °C for 1600 h	319 ± 12 [13]	10.9 ± 1.9 [13]
Al–0.1Zr–0.1Ti(b)		351 ± 10 [13]	11.6 ± 2.3 [13]
Al–0.1Zr(b)	Isothermally aged at 500 °C for 100 h (after 375 °C for 100 h)	325 ± 17 (Fig. 1)	12.3 ± 2.9 (Fig. 5a)
Al–0.1Zr–0.1Ti(b)		319 ± 12 (Fig. 1)	12.0 ± 4.0 (Fig. 5c)
Al–0.1Zr(c)	Isochronally aged to 525 °C	327 ± 13 (Fig. 6)	6.8 ± 1.8 (Table 2)
Al–0.1Zr–0.1Ti(c)		341 ± 8 (Fig. 6)	6.6 ± 1.9 (Table 2)

4.8. Effect of Ti additions

The isothermal (Fig. 1) and isochronal (Fig. 6) hardness curves, as well as the mean precipitate radii presented in Tables 2 and 3, indicate that there is no benefit, in terms of coarsening resistance, of $Al_3(Zr_{1-x}Ti_x)$ ($L1_2$) precipitates as compared to Al_3Zr ($L1_2$). There is, however, a noticeable influence on the incubation time for nucleation, as evidenced in Fig. 6 and also in the isothermal hardness curves of similar alloys at 375–425 °C [13]. Moreover, the peak hardness of Al–0.1Zr–0.1Ti(b) is greater than that of Al–0.1Zr(b) during isothermal aging at 425 °C [13], and that of Al–0.1Zr–0.1Ti(c) is similarly greater than that of Al–0.1Zr(c) during isochronal aging (Fig. 6). The same effect was observed by Sato et al. [39] in chill-cast Al–0.17Zr and Al–0.12Zr–0.15Ti (at.%) alloys aged at 450 °C for up to 1200 h. The Al–0.12Zr–0.15Ti alloy had a reduced incubation time for nucleation and also exhibited a larger peak hardness (400 MPa) value compared to Al–0.17Zr (350 MPa).

The influence of dissolved Ti in α-Al solid solution on AC electrical conductivity is readily apparent in Fig. 6, as the as-cast AC conductivity of Al–0.1Zr–0.1Ti(c) (26.6 ± 0.05 MS m^{-1}) is significantly less than that of Al–0.1Zr(c) (29.7 ± 0.04 MS m^{-1}). The change in AC conductivity between the as-cast and peak-aged conditions is, however, comparable for Al–0.1Zr–0.1Ti(c) and Al–0.1Zr(c), indicating that Zr (the common solute) is the dominant precipitating species, with Ti atoms partitioning weakly to the $Al_3(Zr_{1-x}Ti_x)$ ($L1_2$) precipitates. These observations are consistent with the results of our prior study on similar alloys by atom-probe tomography (APT) [37], where only a small amount of Ti is precipitated from α-Al solid solution in Al–0.1Zr–0.1Ti alloys aged isothermally at 375 or 425 °C, and also the hardness data in a prior microstructural study [13], where the effect of Ti is small compared to that of Zr in dictating the hardness of similar alloys during isothermal aging.

Murray [40] has calculated that Ti additions reduce the solid solubility of Zr in metastable equilibrium with Al_3Zr ($L1_2$). At 400 °C, the solid solubility of Al_3Zr ($L1_2$) is predicted to be 0.011 at.% Zr, whereas the solubility of $Al_3(Zr_{1-x}Ti_x)$ ($L1_2$) precipitates in an Al–0.1Zr–0.1Ti alloy is only 0.005 at.% Zr. At 660 °C, corresponding to the maximum solid solubility, the solid solubility of Al_3Zr ($L1_2$) is

0.172 at.% Zr, while that of $Al_3(Zr_{1-x}Ti_x)$ ($L1_2$) is 0.154 at.% Zr. This increased supersaturation (for a given Zr concentration) accounts for both the reduced incubation time for nucleation in the Al–Zr–Ti alloys and the larger peak strength, since the equilibrium volume fraction of precipitate-rich dendrites is greater. Titanium additions thus have a similar effect as isochronal aging: (i) enhancing the effective supersaturation of Zr during nucleation; and (ii) increasing the volume fraction of the precipitate-rich dendrites. Unfortunately, the variation in apparent dendritic cell size varies considerably throughout the alloy, as discussed previously [13], and there is no practical way to quantify this phenomenon using conventional two-dimensional microscopy, which results in a two-dimensional projection of a three-dimensional microstructure.

4.9. Comparison with prior studies

The present results on Al–Zr and Al–Zr–Ti alloys reaffirm the conclusions of our earlier study [13], which found that transition metal additions (V and/or Ti) to Al–Zr alloys do not improve the coarsening resistance of Al_3Zr ($L1_2$) precipitates. We now compare the present results to those of Malek et al. [41–46], who performed an extensive investigation on the Al–Zr–Ti system in highly supersaturated alloys produced by melt spinning. A series of Al–1.25 at.% $(Zr_{1-x}Ti_x)$ alloys were studied, in which the stoichiometric parameter, x, was progressively varied according to $x = 0$, 0.25, 0.5, 0.75, and 1. Malek et al. claimed that a partial substitution of Ti for Zr in $Al_3(Zr_{1-x}Ti_x)$ improves the stability and also delays the onset of overaging and the $L1_2 \rightarrow D0_{23}$ transformation, as evidenced by both by AC electrical conductivity [45] and Knoop microhardness [46] measurements during isochronal and isothermal aging. With an increasing Ti:Zr ratio, the decomposition of the supersaturated solid solution is shifted to higher temperatures during isochronal aging; the onset of overaging is similarly delayed to higher temperatures with increasing Ti content.

Assuming that Ti partitions slightly to the $Al_3(Zr_{1-x}Ti_x)$ precipitates, then the shift in precipitate nucleation to higher temperatures with increasing Ti content that Malek et al. observed may simply be a kinetic effect, as decreasing the Zr content (the solute species primarily involved in precipitation) reduces the chemical driving force for nucle-

ation and hence increases the incubation time for nucleation. We observed a similar effect, Fig. 6, where the onset of nucleation during isochronal aging is sensitive to the overall supersaturation (our study is different from that of Malek et al. in that we did not vary the Zr content, so in our case the Ti-containing alloy has a larger overall supersaturation and hence exhibits faster incubation kinetics, Fig. 6). Moreover, with increasing Ti:Zr ratio, Malek et al. observed a systematic decrease in the magnitude of the AC electrical conductivity change [45] and precipitation-hardening response [46] accompanying decomposition of supersaturated α-Al during isochronal aging, which is also consistent with our observations that Ti remains mainly in solid solution rather than partitioning to the $Al_3(Zr_{1-x}Ti_x)$ precipitates [37].

5. Conclusions

The temporal evolution of Al_3Zr ($L1_2$) and $Al_3(Zr_{1-x}Ti_x)$ ($L1_2$) precipitates is investigated in conventionally solidified Al–0.1Zr and Al–0.1Zr–0.1Ti (at.%) alloys isothermally aged at 500 °C or isochronally aged from 300 to 600 °C. The following results are obtained and discussed:

- Both alloys overage at the same rate at or above 500 °C (Figs. 1 and 8), during which the metastable Al_3Zr ($L1_2$) or $Al_3(Zr_{1-x}Ti_x)$ ($L1_2$) precipitates coarsen and transform to their respective equilibrium $D0_{23}$ structures. Ternary additions of Ti neither improve the coarsening resistance nor delay the $L1_2 \rightarrow D0_{23}$ transformation. Titanium, however, reduces the incubation time for nucleation and also increases the peak hardness achieved during aging (Fig. 6). These are effects of solute supersaturation (increased chemical driving force for precipitation and precipitate-rich dendrite volume fraction).
- The $L1_2 \rightarrow D0_{23}$ transformation is limited primarily to precipitates heterogeneously nucleated on dislocations and small-angle grain boundaries, which coarsen by dissolution of surrounding $L1_2$ precipitates, probably by rapid pipe diffusion along dislocations. During the transformation, $L1_2$-structured precipitates develop antiphase boundaries (APBs) parallel to $\{100\}$ planes and exhibit preferential growth along $\langle 100 \rangle$ directions (resulting in elongated spheroids), indicating a transition to an imperfect equilibrium $D0_{23}$ structure.
- The equilibrium $D0_{23}$ structure exhibits a disk-shaped morphology, ca. 200 nm in diameter and 50 nm in thickness, exhibiting a cube-on-cube orientation relationship with the α-Al solid solution. The disk-shaped morphology of the equilibrium phase reflects the tetragonal symmetry of the $D0_{23}$ unit cell.
- Precipitation strengthening in segregated Al–Zr alloys occurs on two length scales: (i) on the nanometer-scale by an Orowan strengthening mechanism; and (ii) on the micrometer-scale related to the volume fraction of the precipitate-rich dendrites. Microstructural coarsening similarly occurs on two length scales: (i) by Ostwald ripening of spheroidal nanometer-scale precipitates within the dendrites; and (ii) by local dissolution of the micrometer-scale precipitate-rich dendrites during the $D0_{23}$ transformation.
- Because strengthening depends on the volume fraction of the precipitate-rich dendrites, thermal history has a strong influence on the observed alloy strength. During isochronal aging (Fig. 6), Vickers microhardness values of the order of 415 MPa may be obtained for Al–0.1Zr (at.%) after aging up to 450 °C; during isothermal aging, the attainable hardness at 425 °C is only ca. 300 MPa [13]. Unlike isothermal aging, isochronal aging nucleates precipitates at the lowest possible aging temperature, where the solute supersaturation and chemical driving force are greatest, resulting in: (i) smaller precipitates, since the critical radius for nucleation is reduced; and (ii) a larger volume fraction of precipitate-rich dendrites since the supersaturation is greatest at lower temperatures.

References

[1] Knipling KE, Dunand DC, Seidman DN. Z Metallkd 2006;97:246.
[2] Knipling KE, Dunand DC, Seidman DN. Metall Mater Trans A 2007;38:2552.
[3] Westbrook JH. Superalloys (Ni-base) and dislocations – an introduction. In: Nabarro FRN, Duesberry MS, editors. $L1_2$ ordered alloys, vol. 10. Amsterdam: Elsevier; 1996. p. 1.
[4] Reed RC. The superalloys: fundamentals and applications. Cambridge (UK): Cambridge University Press; 2006.
[5] Fine ME. Metall Trans A 1975;6:625.
[6] Angers LM, Chen YC, Fine ME, Weertman JR, Zedalis MS. Rational design of high temperature aluminum alloys. In: Starke EA, Sanders TH, editors. Aluminum alloys: their physical and mechanical properties, vol. 1. Warley (UK): EMAS; 1986. p. 321.
[7] Zedalis MS, Fine ME. Metall Trans A 1986;17:2187.
[8] Fine ME. Stability and coarsening of dispersoids in aluminum alloys. In: Kim YW, Griffith WM, editors. Dispersion strengthened aluminum alloys. Warrendale (PA): TMS; 1988. p. 103.

[9] Lewis RE, Crooks DD, Chen YC, Fine ME, Weertman JR. High temperature Al–Zr–V alloys using rapid solidification processing. In: Wilshire B, Evans RW, editors. Proceedings of the 3rd international conference on creep and fracture of engineering materials and structures. London (UK): The Institute of Metals; 1987. p. 331.

[10] Chen YC, Fine ME, Weertman JR, Lewis RE. Scripta Metall 1987;21:1003.

[11] Chen YC, Fine ME, Weertman JR. Acta Metall Mater 1990;38:771.

[12] Parameswaran VR, Weertman JR, Fine ME. Scripta Metall 1989;23:147.

[13] Knipling KE, Dunand DC, Seidman DN. Acta Mater 2008;56:114.

[14] Balluffi RW, Allen SM, Carter WC. Kinetics of materials. Hoboken: John Wiley & Sons; 2005.

[15] Zuo JM, Mabon JC. Web-based electron microscopy application software: Web-EMAPS. Microsc Microanal 2004;10(Suppl. 2):1000. <http://emaps.mrl.uiuc.edu/>.

[16] Chen Y-C. PhD Thesis, Materials Science and Engineering Department, Northwestern University, 1988.

[17] Lee HS, Han SZ, Lee HM, Lee ZH. Mater Sci Eng A 1993;163:81.

[18] Ryum N. J Mater Sci 1975;10:2075.

[19] Cahn JW, Kalonji G. Symmetry in solid state transformation morphologies. In: Aaronson HI, Laughlin DE, Sekerka RF, Wayman CM, editors. Proceedings of an international conference on solid-solid phase transformations. Warrendale (PA): The Metallurgical Society of AIME; 1982. p. 3.

[20] Izumi O, Oelschlägel D. Scripta Metall 1969;3:619.

[21] Nes E. Acta Metall 1972;20:499.

[22] Ryum N. Acta Metall 1969;17:269.

[23] Dahl W, Gruhl W, Burchard WG, Ibe G, Dumitrescu C. Z Metallkd 1977;68:188.

[24] Srinivasan S, Desch PB, Schwarz RB. Scripta Metall Mater 1991;25:2513.

[25] Brown LM, Ham RK. Strengthening methods in crystals. London: Elsevier Publishing Company; 1971.

[26] Ardell AJ. Metall Trans A 1985;16:2131.

[27] Ardell AJ. Ch. 12: Intermetallics as precipitates and dispersoids in high-strength alloys. In: Westbrook JH, Fleischer RL, editors. Intermetallic compounds: principles and practice, vol. 2. Chichester: John Wiley & Sons; 1994. p. 257.

[28] Meyers MA, Chawla KK. Mechanical metallurgy: principles and applications. NJ: Prentice-Hall; 1984.

[29] Frost HJ, Ashby MF. Deformation-mechanism maps: the plasticity and creep of metals and ceramics. New York: Pergamon Press; 1982.

[30] Nembach E. Particle strengthening of metals and alloys. New York (NY): John Wiley & Sons; 1997.

[31] Knipling KE. PhD Thesis, Materials Science and Engineering Department, Northwestern University, 2006. Available from: http://arc.nucapt.northwestern.edu/refbase/show.php?record=1785.

[32] Seidman DN, Marquis EA, Dunand DC. Acta Mater 2002;50:4021.

[33] Fuller CB, Seidman DN, Dunand DC. Acta Mater 2003;51:4803.

[34] Marquis EA, Seidman DN, Dunand DC. Acta Mater 2003;51:4751.

[35] van Dalen ME, Dunand DC, Seidman DN. Acta Mater 2005;53:4225.

[36] van Dalen ME, Dunand DC, Seidman DN. J Mater Sci 2006;41:7814.

[37] Knipling KE, Dunand DC, Seidman DN. Microsc Microanal 2007;13:503.

[38] Tabor D. Br J Appl Phys 1956;7:159.

[39] Sato T, Kamio A, Lorimer GW. Mater Sci Forum 1996;217–222:895.

[40] Murray JL. Personal communication; 2006.

[41] Malek P, Janecek M, Smola B, Bartuska P. Key Eng Mat 1994;97–98:65.

[42] Malek P, Janecek M, Smola B, Bartuska P, Plestil J. J Mater Sci 2000;35:2625.

[43] Malek P, Bartuska P, Plestil J. Kovové Mater 1999;37:386.

[44] Malek P, Janecek M, Smola B, Bartuska P. Kovové Mater 2000;38:9.

[45] Malek P, Chalupa B, Plestil J. Kovové Mater 2000;38:77.

[46] Malek P, Janecek M, Smola B. Kovové Mater 2000;38:160.